

LWS observations of the colliding galaxies NGC 4038/39*

J. Fischer^{1,16}, L.M. Shier¹, M.L. Luhman¹, S. Satyapal^{2,16}, H.A. Smith², G.J. Stacey³, S.J. Unger⁴, M.A. Greenhouse², L. Spinoglio⁵, M.A. Malkan⁶, S.D. Lord⁷, J.W. Miles², M.A. Shure^{8,16}, P.E. Clegg⁹, P.A.R. Ade⁹, C. Armand¹⁰, M. Burgdorf¹⁰, S.E. Church¹¹, G.R. Davis¹², A. Di Giorgio¹⁰, D. Ewart¹⁰, I. Furniss¹³, W.M. Glencross¹³, C. Gry^{10,14}, T. Lim¹⁰, S. Molinari¹⁰, Q. Nguyen-Rieu¹⁵, M.C. Price¹⁰, S.D. Sidher¹⁰, A. Smith¹⁰, B.M. Swinyard⁴, D. Texier¹⁰, N.R. Trams¹⁰, and M.G. Wolfire²

¹ Naval Research Laboratory, Remote Sensing Division, 4555 Overlook Avenue, SW, Washington, DC 20375, USA

² National Air and Space Museum, Smithsonian Institute, Laboratory for Astrophysics, Washington, DC 20560, USA

³ Cornell University, Astronomy Dept., 230 Space Sciences Bldg., Ithaca, NY 14853, USA

⁴ Rutherford Appleton Laboratory, S and A Division, Chilton, Didcot, Oxfordshire OX11-0QX, UK

⁵ CNR-Istituto di Fisica dello Spazio Interplanetario, Casella Postale 27, I-00044 Frascati (Rome), Italy

⁶ University of California, Dept. of Astronomy, Los Angeles, CA 90024, USA

⁷ California Institute of Technology, IPAC, Pasadena, CA 91125, USA

⁸ Georgia State Univ., Ctr. High Angular Res. Astro., 38 Peachtree Ctr. Ave. 1039GCB, Atlanta, GA 30303, USA

⁹ Queen and Mary Westfield College, Univ. of London, Dept. of Physics, Mile End Road, London E1-4NS, UK

¹⁰ The LWS Instrument-Dedicated Team, ISO Science Operations Centre, PO Box 50727, Madrid, Spain

¹¹ California Institute of Technology, Division of Physics, Math, and Astronomy, MS-59-33, Pasadena, CA 91125, USA

¹² Institute of Space and Atmospheric Studies, Univ. of Saskatchewan, 116 Science Pl., Saskatoon, Sask. S7N 5E2, Canada

¹³ University College London, Univ. of London, Dept. of Physics and Astronomy, Gower Street, London WC1E-6BT, UK

¹⁴ Laboratoire d'Astronomie Spatiale, CNRS, BP 8, F-13248 Marseille Cedex 12, France

¹⁵ Observatoire de Paris, 61 Avenue de l'Observatoire, F-75014 Paris, France

¹⁶ Visiting Astronomer at the Infrared Telescope Facility, which is operated by the Univ. of Hawaii under contract from NASA

Received 1 July 1996 / Accepted 2 August 1996

Abstract. Infrared Space Observatory (ISO) Long Wavelength Spectrometer (LWS) and ground-based Fabry-Perot imaging spectroscopic observations are used to penetrate the extinction to the powerful burst of star formation that has occurred in the extranuclear molecular cloud complex in the galaxy overlap region of the galaxies NGC 4038/39 ("The Antennae"). Parameters of the starburst and typical molecular cloud core characteristics are derived. It is found that the starburst can power the infrared luminosity of this galaxy system.

Key words: infrared: galaxies – galaxies: interactions – galaxies: starburst – galaxies: evolution – galaxies: nuclei – galaxies: individual NGC 4038/39

1. Introduction

One of the most important discoveries resulting from IRAS was that many galaxies emit a large fraction of their energy in the far infrared and that a significant number of these have luminosities of $10^{12} L_{\odot}$ or more (Soifer et al. 1987). Many of these

galaxies appear to be colliding or merging pairs. Theories on the role played by mergers in galaxy evolution are consistent with a variety of origins for the high infrared luminosity observed in mergers, e.g. shocks produced by cloud-cloud collisions, exceptional bursts of star formation, or reradiation by dust surrounding a hidden active galactic nucleus. In all of these scenarios, the presence of copious amounts of gas and dust renders attempts to determine the dominant physical processes and the embedded stellar content a challenging endeavor. Far infrared spectroscopy is a tool well suited to this task.

In this paper we present ISO/LWS observations of NGC 4038/39, a pair of galaxies thought to be in the early stages of merging. We also present ground-based near infrared Fabry-Perot imaging spectroscopy of this system in order to help determine the spatial origin and excitation of the lines detected by the LWS.

2. The Observations and Results

The ISO/LWS (Clegg et al. 1996) was operated in its low resolution ($R \equiv \lambda/\Delta\lambda \sim 200$) mode to obtain spectral line scans of seven far infrared forbidden fine structure transitions on 19 January 1996. ISO was pointed at the position R.A.(1950)=11^h 59^m 20^s Dec(1950)=-18°35'51" so that the LWS beam (Swinyard et al. 1996) encompassed the extranuclear molecular cloud

Send offprint requests to: J. Fischer, jfischer@irfp8.nrl.navy.mil

* Based on observations with ISO, an ESA project with instruments funded by ESA Member States (especially the PI countries: France, Germany, the Netherlands and the United Kingdom) and with the participation of ISAS and NASA.

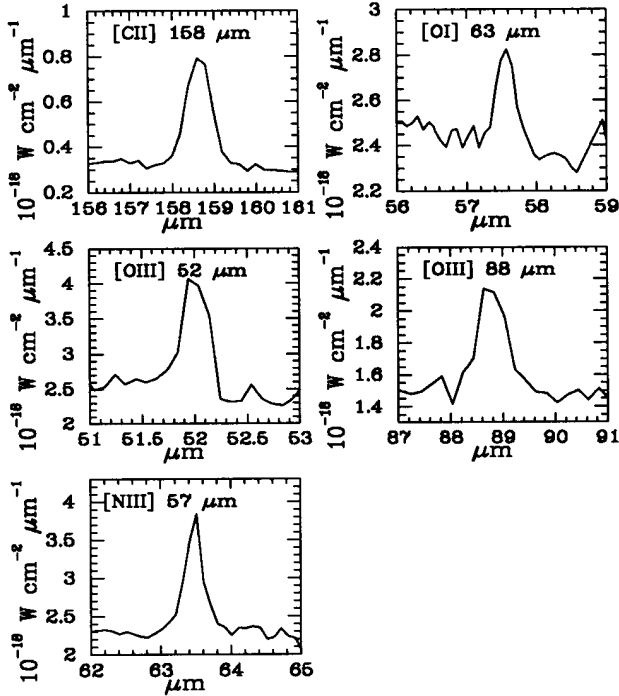


Fig. 1. Spectra of emission lines detected by LWS.

complex in the galaxy overlap region (Stanford et al. 1990) as well as the nuclei of both galaxies. Because data are simultaneously obtained for all ten detector bands, almost the entire LWS range was covered. The calibration accuracy of individual detectors was estimated to be $\pm 30\%$ based on overlapping data in neighboring detectors. An attempt was made to correct for these systematic errors by fitting the line free parts of the continuum with a second-order polynomial in the $\log F_\lambda - \log \lambda$ plane. The sub-spectra of individual detectors were then scaled so that their averages lay on this polynomial. Five of the seven lines observed were detected. The line spectra are shown in Figure 1. The derived line fluxes, their statistical uncertainties (small compared with the calibration accuracy), and 3σ upper limits for undetected lines are given in Table 1.

High spatial resolution Fabry-Perot $2 \mu\text{m}$ spectroscopy was obtained using the NRL/NASM Fabry-Perot spectrometer interfaced to the NASA IRTF camera NSFCAM. The pixel size was $0.3''$ per pixel and the spectral resolution was $R \simeq 800$. The $\text{Br}\gamma$ and $\text{H}_2 \nu=1-0 \text{ S}(1)$ line images of the nuclear region of NGC 4039 and the extranuclear molecular cloud complex are shown in Figures 2 and 3 respectively. Integrated intensity contours of $\text{CO}(1-0)$ from the aperture synthesis observations of Stanford et al. (1990) are superposed on the two line images for reference. The images were registered with respect to the CO interferometry using the infrared position of the nucleus: R.A.(1950) = $11^{\text{h}} 59^{\text{m}} 19^{\text{s}}.7$ Dec(1950) = $-18^\circ 36' 27'' (\pm 2-3'')$ (S.A. Stanford, priv. comm.). Clumps of $\text{Br}\gamma$ emission and a diffuse level of line emission are located in and around the extranuclear region. The brightest of the $\text{Br}\gamma$ sources are associated with each of the four velocity components that make up the extranuclear cloud and

Table 1. Emission Line Fluxes

Emission line	Line Flux $10^{-19} \text{ W cm}^{-2}$	Statistical Error (1σ) $10^{-20} \text{ W cm}^{-2}$
[OIII] $52 \mu\text{m}$	4.9	2.9
[NIII] $57 \mu\text{m}$	1.6	0.58
[OI] $63 \mu\text{m}$	5.2	1.1
[OIII] $88 \mu\text{m}$	4.7	1.3
[NII] $122 \mu\text{m}$	< 0.44 (3σ)	
[OI] $146 \mu\text{m}$	< 0.25 (3σ)	
[CII] $158 \mu\text{m}$	3.7	0.51
$\text{Br}\gamma$ $2.16 \mu\text{m}$	0.67	
H_2 $1-0 \text{ S}(1)$ $2.12 \mu\text{m}$	0.12	

with $\text{H}\alpha$ and radio knots (Bushouse 1987; Hummel & van der Hulst 1986). Faint clumps of $\text{H}_2 \nu=1-0 \text{ S}(1)$ line emission are coincident with three of the $\text{Br}\gamma$ sources. The $\text{Br}\gamma$ and $\text{S}(1)$ line fluxes in a $30''$ aperture including the NGC 4039 nucleus and sources to the northeast are given in Table 1. Approximately 70% of this emission is diffuse.

3. Discussion

3.1. The Ionized Gas and Starburst Parameters

The presence of strong $\text{Br}\gamma$ emission in and around the extranuclear cloud provides evidence that a localized starburst has occurred in this region. The [NIII], [OIII], [NII], and $\text{Br}\gamma$ observations can be used to constrain the age of the burst, assuming solar abundances. The CLOUDY computer code (Ferland 1993) was run with a single star model to assign characteristic ionized gas properties and an effective stellar temperature for the stars responsible for the ionization. The observed line fluxes are fitted, within $\pm 2.5\sigma$, by a single star effective temperature in the range $(3.9 - 4.0) \times 10^4 \text{ K}$. The derived electron density and temperature ranges, $n_e = 60 - 400 \text{ cm}^{-3}$ and $T_e = 7000 \pm 1000 \text{ K}$, imply an HII region pressure range of $P_{\text{HII}}/k = (0.4 - 3) \times 10^6 \text{ K cm}^{-3}$.

To derive the parameters of the starburst, an evolutionary synthesis code (Leitherer & Heckman 1995) was used to compute the starburst spectral energy distribution for input to CLOUDY. For an instantaneous burst with a Salpeter IMF ($\alpha = -2.35$) for masses $0.1 - 100 M_\odot$, line fluxes were calculated as a function of the age of the starburst.

In Figure 4 the logarithm of the ratio of the $\text{Br}\gamma$ to [OIII] $52 \mu\text{m}$ line is plotted as a function of the burst age to illustrate the dependence of the derived burst age on the observed line ratio and extinction. For the compact $\text{Br}\gamma$ sources in the extranuclear cloud, we derive $A_V = 1 - 4$ from both the $\text{Br}\gamma/\text{H}\alpha$ ratio using $\text{H}\alpha$ images from Bushouse et al. (1987) and the measured versus predicted $\text{H}\alpha$ fluxes from the radio results of Hummel & van der Hulst (1986), while Kunze et al. (1996) derive $A_V = 70$ for a model with mixed gas and dust from $\text{Br}\alpha/\text{Br}\beta$. Figure 4 illustrates that because strong [OIII] line emission is limited to the most massive and short lived stars, the age of an instantaneous burst is well constrained by the $\text{Br}\gamma/[\text{OIII}]52 \mu\text{m}$ line ratio to $7 - 8 \times 10^6 \text{ yr}$, even allowing for a large range in the extinction and

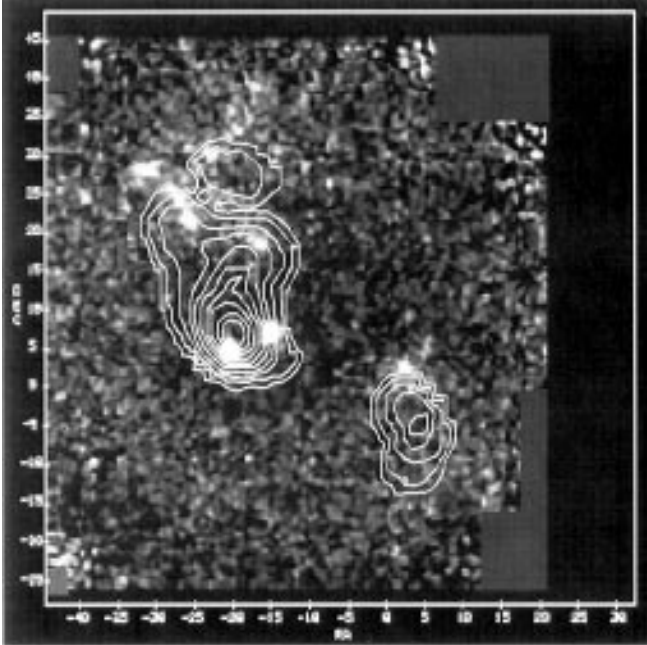


Fig. 2. $\text{Br}\gamma$ line Fabry-Perot image with CO(1-0) aperture synthesis contours from Stanford et al. (1990).

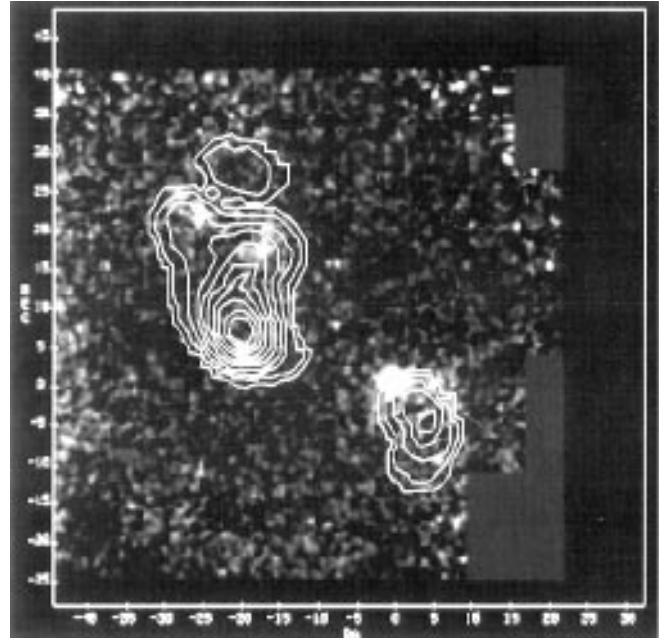


Fig. 3. H_2 1-0 S(1) line Fabry-Perot image with CO(1-0) aperture synthesis contours from Stanford et al. (1990).

some $\text{Br}\gamma$ contribution from outside of our Fabry-Perot image. The other LWS line ratios are also consistent with this value. Although we find that a starburst with continuous star formation with the same IMF is not consistent with the observed line fluxes, a finite rather than instantaneous duration burst could help explain the age of the youngest clusters (age $\sim 4 \times 10^6$ yr) indicated by the $\text{Br}\gamma$ equivalent widths of some of the compact $\text{Br}\gamma$ sources (Fischer et al. 1996) and by the blue colors seen by Whitmore & Schweizer (1995). Based on the far infrared line fluxes and an adopted distance of 26 Mpc ($V_{\text{LSR}}=1550 \text{ km s}^{-1}$ and $H_0=60 \text{ km s}^{-1} \text{ Mpc}^{-1}$) the total stellar mass produced by the instantaneous burst is $\sim (2.5 \pm 1.5) \times 10^8 M_\odot$ and its luminosity is $(7 \pm 4) \times 10^{10} L_\odot$. This is about equal to the far infrared luminosity (to within the uncertainties) in the LWS beam (see below), indicating that the far infrared luminosity is powered by star formation in this system.

3.2. The Dust and Warm, Neutral Gas

The LWS continuum was obtained by averaging data from all line scans and the associated multiplexed data. The continuum is best fit with a ν^{-1} emissivity law and a dust temperature $T_d=41 \text{ K}$, a typical value for starburst galaxies (Stacey et al. 1991). The derived total IR luminosity within the LWS beam is $3.9 \times 10^{10} L_\odot$. The derived temperature and emissivity law agree well with that of Soifer et al. (1987). The total luminosity is lower than that found by Soifer et al. due to the smaller distance adopted here and the smaller flux within the LWS aperture compared with the larger total IRAS flux.

Since the peak wavelength of the observed [CII] line is at the expected redshifted value for the Antennae, we conclude

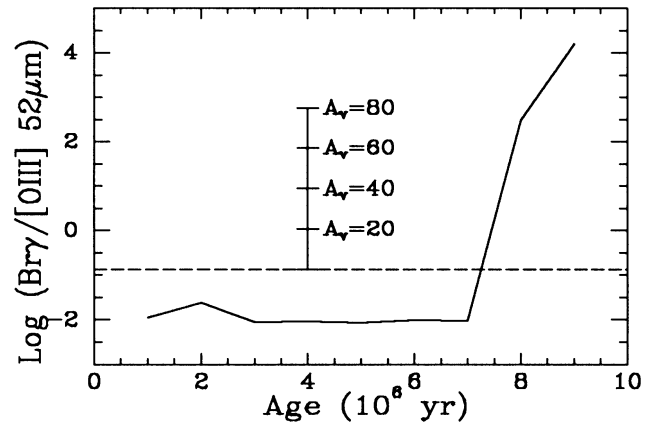


Fig. 4. $\text{Log}(\text{Br}\gamma \text{ line}/[\text{OIII}] 52 \mu\text{m} \text{ line})$ as a function of starburst age for the instantaneous burst discussed in the text. The dashed line indicates the measured line ratio from Table 1.

that the observed emission is not significantly contaminated by galactic emission. The near unity value of the [CII] $158 \mu\text{m}/[\text{OI}] 63 \mu\text{m}$ ratio and the high [OI] $63 \mu\text{m}/[\text{OI}] 146 \mu\text{m}$ ratio (> 19) provide strong evidence that the [CII] and [OI] lines arise in photodissociation regions (PDRs). We derived the PDR physical conditions and typical cloud properties following the analysis of Wolfire et al. (1990) (see Table 2), using a molecular mass of $1.84 \times 10^9 M_\odot$ for the extranuclear region (Stanford et al. 1990, scaled to our adopted distance). The range of pressures derived for the PDRs are consistent with the pressure range derived for the HII regions, indicating possible near pressure balance between the HII regions and the neutral medium. The derived typical parameters of the warm, neutral medium in the Antennae are similar to other starburst galaxies (eg. M82, Lord

et al. 1996). The Antennae system falls in the range of moderate starburst galaxies on the plot of Stacey et al. (1991) with an overall [CII]/CO line intensity value of 2500. The young OB stars must be in close proximity to the clouds since from Table 2 the UV field incident on the clouds is high compared with the average UV field, consistent with recent star formation activity.

3.3. Excitation of the H₂ Line Emission

For moderately dense ($n \leq 10^4 \text{ cm}^{-3}$) clouds exposed to UV photons from nearby OB stars where $G_o \leq 10^4$, the H₂ v=1-0 S(1) line and far infrared continuum emission are well correlated (Luhman & Jaffe 1996). If the H₂ emission in NGC 4038/39 arises in UV exposed gas (PDRs), then applying this correlation to the ISO far infrared flux (scaled to the derived area filling factor in Table 2) yields $[I_{S(1)}]_{PDR} = \text{a few} \times 10^{-5} \text{ erg s}^{-1} \text{ cm}^{-2} \text{ sr}^{-1}$. The brightest H₂ emission is found at the NGC 4039 nucleus (first detected at both nuclei in large aperture observations by Campbell & Willner 1989). The surface brightness there is $I_{S(1)} = 8 \times 10^{-5} \text{ erg s}^{-1} \text{ cm}^{-2} \text{ sr}^{-1}$, four times higher than the PDR relationship would predict. In contrast, in the Br γ image only a faint unresolved source is seen $\sim 3''$ northwest of the NGC 4039 nucleus. We therefore argue that in the nucleus of NGC 4039, the emission is probably due to shocks. These shocks are most likely C-shocks since the measured S(1) and Br γ flux levels at the nucleus are inconsistent with J-shock models (Hollenbach & McKee 1989). Does this indicate that some of the [OI] 63 μm flux in the LWS beam is excited by shocks? Probably not. Based on the observed (uncorrected) S(1) line strength, C-shock models indicate that for most shock velocities, [OI] 63 μm emission would be small compared with the flux level observed with the LWS (Draine et al. 1983).

The faint peaks of S(1) line emission in and around the extranuclear cloud region have surface brightnesses $I_{S(1)} \simeq 2 - 4 \times 10^{-5} \text{ erg s}^{-1} \text{ cm}^{-2} \text{ sr}^{-1}$, consistent with UV excitation. We argue therefore that these H₂ emission regions and perhaps others more deeply embedded in the extranuclear cloud complex are the likely sites of the [CII] and [OI] PDR emission detected

by the LWS. These results are also consistent with the location of the Br γ sources in the extranuclear region.

References

- Bushouse, H.A. 1987, ApJ, 320, 49
 Campbell, A., Willner, S.P. 1989, AJ, 97, 995
 Clegg, P.E., Ade, P.A.R., et al. 1996, A & A, this issue
 Draine, B.T., Roberge, W.G., et al. 1983, ApJ, 264, 485
 Ferland, G.J. 1993, Univ. of Kentucky Depart. of Phys. & Astron. Internal Rep.
 Fischer, J., Satyapal, S., et al. 1996, ApJ, in prep.
 Hollenbach, D., McKee, C.F. 1989, ApJ, 342, 306
 Hummel, E., van der Hulst, J.M. 1986, A & A, 155, 151
 Kunze, D., Rigopoulou, D., et al. 1996, A & A, this issue
 Leitherer, C., Heckman, T.M. 1995, ApJS, 96, 9
 Lord, S.D., Hollenbach, D.J., et al. 1996, ApJ, 465, 703
 Luhman, M.L., Jaffe, D.T. 1996, ApJ, 463, 191
 Soifer, B.T., Sanders, D.B., et al. 1987, ApJ, 320, 238
 Stacey, G.J., Geis, N., et al. 1991, ApJ, 373, 423
 Stanford, S.A., Sargent, A.I., et al. 1990, ApJ, 349, 492
 Swinyard, B.M., Clegg, P.E., et al. 1996, A & A, this issue
 Whitmore, B., Schweizer, F. 1995, AJ, 109, 960
 Wolfire, M.G., Tielens, A.G.G.M., et al. 1990, ApJ, 358, 116

Table 2. PDR and typical cloud properties

Physical Condition or Size	Derived Values
n_{PDR}	$(0.25 - 1.5) \times 10^4 \text{ cm}^{-3}$
G_o , UV field flux	200 - 2500 \times local ISRF
T_{PDR}	$200 \pm 60 \text{ K}$
P_{PDR}/k	$(0.35 - 3.9) \times 10^6 \text{ K cm}^{-3}$
M_{PDR}	$8.4 \times 10^7 M_{\odot}$
Φ_A , area filling factor	0.04 ± 0.01
Φ_V , volume filling factor	1.8×10^{-5}
r_{core} , molecular core radius	2.32 pc
Thickness of PDR surface layer	0.03 pc
N_{cloud} , number of clouds	1.8×10^5
M_c , cloud core mass	$10^4 M_{\odot}$ (per cloud)
$\langle G_o \rangle_{ISRF}$, average ISRF	45 \times local ISRF